

Article

High-Performing Au-Ag Bimetallic Catalysts Supported on Macro-Mesoporous CeO₂ for Preferential Oxidation of CO in H₂-Rich Gases

Roberto Fiorenza ^{1,*}, Luca Spitaleri ^{1,2}, Antonino Gulino ^{1,2} and Salvatore Scire ¹

¹ Department of Chemical Sciences, University of Catania, Viale A. Doria 6, 95125 Catania, Italy; lucaspatialeri@hotmail.it (L.S.); agulino@dipchi.unict.it (A.G.); sscire@unict.it (S.S.)

² I.N.S.T.M. UdR of Catania, Viale A. Doria 6, 95125 Catania, Italy

* Correspondence: rfiorenza@unict.it; Tel.: +39-3936-586-864

Received: 28 November 2019; Accepted: 23 December 2019; Published: 1 January 2020



Abstract: We report here an investigation on the preferential oxidation of carbon monoxide in an H₂-rich stream (CO-PROX reaction) over mono and bimetallic Au-Ag samples supported on macro-mesoporous CeO₂. The highly porous structure of ceria and the synergistic effect, which occurs between the bimetallic Au-Ag system and the support, led to promising catalytic performance at low temperature (CO₂ yield of 88% and CO₂ selectivity of 100% at 60 °C), which is suitable for a possible application in the polymer electrolyte membrane fuel cell (PEMFC). The morphological, structural, textural and surface features of the catalysts were determined by Scanning Electron Microscopy (SEM), Transmission Electron Microscopy (TEM), N₂-adsorption-desorption measurements, Temperature Programmed Reduction in hydrogen (H₂-TPR), Fourier Transform Infrared Spectroscopy (FTIR) and X-ray Photoelectron Spectroscopy (XPS). Furthermore, the catalytic stability of the best active catalyst, i.e., the AuAg/CeO₂ sample, was evaluated also in the presence of water vapor and carbon dioxide in the gas stream. The excellent performances of the bimetallic sample, favored by the peculiar porosity of the macro-mesoporous CeO₂, are promising for possible scale-up applications in the H₂ purification for PEM fuel cells.

Keywords: H₂ purification; PROX reaction; 3DOM structure; bimetallic catalysts; gold; silver

1. Introduction

In the last few years, polymer electrolyte membrane fuel cells (PEMFC), due to their appealing features such as a low working temperature range (60–100 °C) and high energy efficiency [1,2], emerged as a promising reply to the increasing request of renewable and green energy [3,4]. The hydrogen fuel of PEMFC mainly comes from reformat gases through the steam reforming reaction followed by water-gas shift. To avoid the poisoning of the PEMFC platinum anode, which occurs even with trace of CO gas (less than 10 ppm), it is necessary for a pre-treatment step to purify hydrogen from CO [5]. In this context, one of the most used pieces of technology used to obtain a “CO-free” hydrogen source is the preferential oxidation of CO (CO-PROX) [6–8]. The choice of a suitable catalyst for the CO-PROX reaction is fundamental to selectively favor the carbon monoxide oxidation (CO + 1/2 O₂ → CO₂) instead of the hydrogen one (H₂ + 1/2 O₂ → H₂O). The supported platinum group metal catalysts (Pt, Pd, Ru, Rh) efficiently fulfil the requirement of the PROX reaction, especially at high temperatures [7,9–13], but a more economical and performing alternative is represented by the copper-based catalysts [14–18]. Among the various supports utilized, cerium oxide (i.e., ceria, CeO₂) has a predominant role in the PROX reaction, due to its remarkable redox and oxygen storage capacities [12–21].

Compared to the Pt or copper-based catalysts, the Au ones, when the size of gold particles is smaller than 5 nm, are highly active at low temperatures (i.e., below 100 °C), thus matching the operation temperatures required by the PEMFC [22–25]. Furthermore, the high dispersion and the strong interaction over ceria-supported systems allows us to exploit a very high mobility (i.e., reducibility) of the cerium oxide surface oxygen, thus boosting the catalytic activity in the PROX reaction [26–28]. However, the gold-based catalysts suffer some drawbacks, such as rapid deactivation at high temperatures and high sensitivity to moisture [29,30]. To overcome these disadvantages, the addition of other metals, such as Ag [31–34] or Pt [35], to gold leads us to profit from the synergistic interaction between the two metals with the formation of new phases or alloys that can exhibit better activity with respect to the monometallic catalysts.

Other strategies to further enhance the performance of the Au/CeO₂ catalyst in the PROX reaction are the modification of the chemico-physical properties of cerium oxide with the addition of doping agents [36,37], the formation of a CeO₂-composite or mixed oxides [12,38] or, as a new approach, the synthesis of three dimensionally ordered macro-mesoporous (3DOM) CeO₂. The huge pore volume, the regular pore structure, the ordered channel network, the tunable pore size and the good penetrability of 3DOM CeO₂ favor a good adsorption of the reactant gases, and also facilitate the mass transfers [39–42]. All these features contribute to enhancing the performance of gold-supported ceria catalysts.

In this work, for the first time, we carried out an original study on the influence of the addition of Au-Ag nanoparticles to the 3DOM CeO₂, analyzing both the physico-chemical properties of the synthesized materials and their catalytic activity in the PROX reaction.

2. Results

2.1. Morphological, Textural and Structural Properties

The peculiar morphology of the macro-mesoporous ceria is clearly visible from the Scanning Electron Microscopy (SEM) images (Figure 1). The addition of gold and/or silver did not alter the morphology of the support. The interconnected pores can be also observed in the Transmission Electron Microscopy (TEM) pictures (Figure 2a). In Au/CeO₂, Ag/CeO₂ and AuAg/CeO₂, due to the high dispersion (mean sizes of 4 nm) and/or the low amount of the metals on the support, the metal nanoparticles are not easily detectable even at high magnification (see Figure 2b showing the Au/CeO₂ catalyst as a representative sample and Figure S1a,b displaying the HRTEM of Ag/CeO₂ and AuAg/CeO₂). However, the obtained lattice spacing value of AuAg/CeO₂ is larger ($d = 0.240$) than both Au/CeO₂ ($d = 0.235$) and Ag/CeO₂ ($d = 0.236$). In accordance with the literature, this points to the possible formation of a random alloy of gold and silver [31–33,43,44].

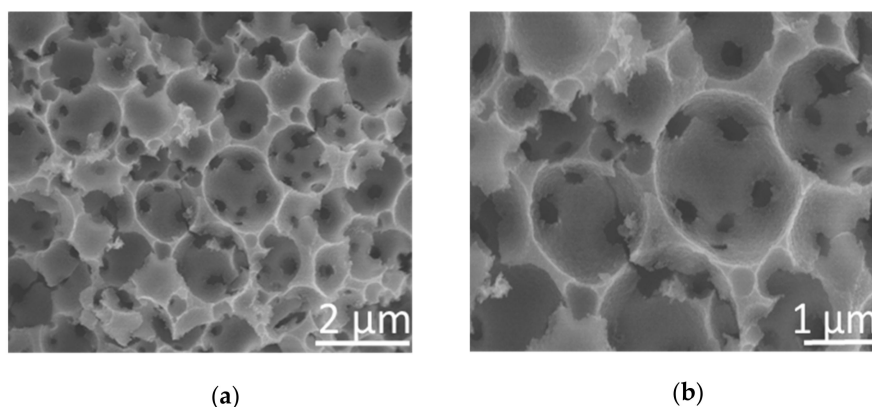


Figure 1. (a) Scanning Electron Microscopy images of the macro-mesoporous CeO₂. (b) Close inspection that evidences the interconnected pores.

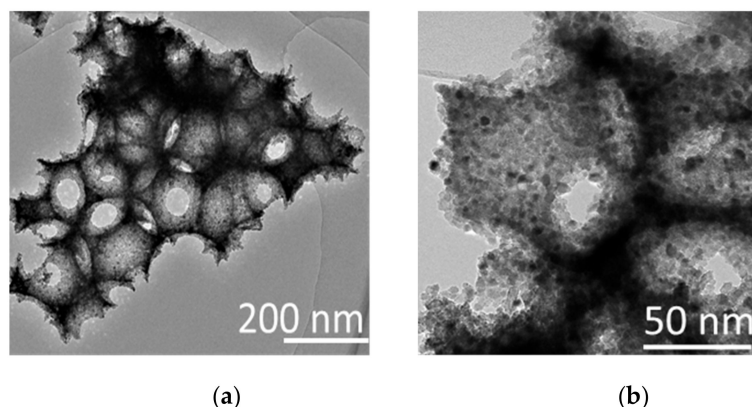


Figure 2. (a) Transmission Electron Microscopy image of the macro-mesoporous CeO₂ support. (b) Close inspection of the Au/CeO₂ sample.

The textural properties of the samples are reported in the Table 1 and Figure 3. All the catalysts exhibited a N₂ adsorption-desorption isotherm of type II–III with a H3 hysteresis loop at high relative pressure (0.5–1.0 p/p_0), typical of the macroporous samples with slit-shaped pores [45]. It is interesting to note that the addition of metals to the macro-mesoporous CeO₂ caused a decrease of the Brunauer-Emmett-Teller (BET) surface area (from 102 to 88–81 m²/g) with a consequent increase in the mean pore diameters from about 5 nm of the pure ceria support to 12–13 nm of the metals/CeO₂. These variations in the textural properties due to the addition of the mono or bimetallic species led to different Barrett, Joyner and Halenda (BJH) pore size distribution curves (Figure 3b). It can be seen that the presence of gold, silver and gold-silver shifts the maximum of the BJH curve at higher pore diameters compared to the CeO₂ support. In particular, whereas the Ag/CeO₂ and AuAg/CeO₂ samples displayed a similar curve, the Au/CeO₂ showed a major presence of macropores (>40 nm) with a wider maximum BJH when compared to the other samples. The inclusion of the noble metals in the macro channels of CeO₂ and the high dispersion of these in the support probably determined these textural properties variations. The high dispersion of the metals on the CeO₂ was further confirmed by the X-ray powder diffraction (XRD) patterns (Figure S2), which always present the characteristic diffractions peaks of the cerium oxide in the fluorite form. The absence of signals ascribed to the noble metals implies that, as confirmed by high resolution TEM (HRTEM), Au and Ag are highly dispersed on the support.

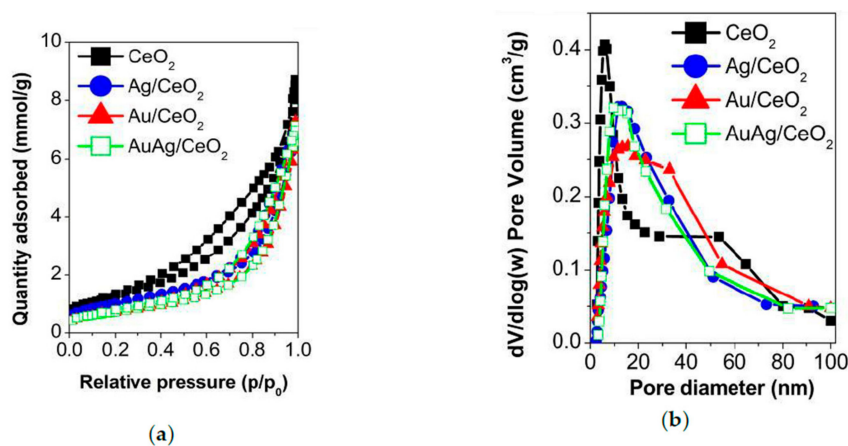
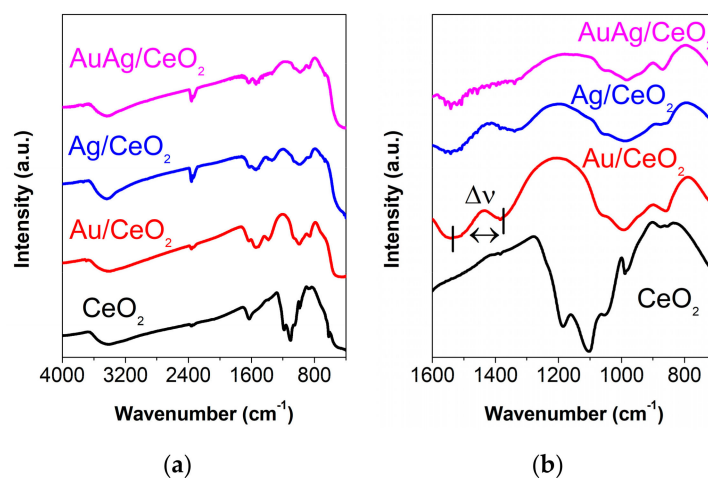


Figure 3. (a) N₂ adsorption-desorption isotherms and (b) Barrett, Joyner and Halenda pore size distribution of the investigated samples.

Table 1. Textural features of the examined catalysts.

Sample	BET Surface Area (m ² /g)	Mean Pore Diameter (nm)	Pore Volume (cm ³ /g)
CeO ₂	102	4.8	0.21
Ag/CeO ₂	81	13.3	0.30
Au/CeO ₂	86	11.3	0.37
AuAg/CeO ₂	88	11.8	0.37

Figure 4a displays the Fourier Transform Infrared Spectroscopy (FTIR) spectra of the investigated catalysts. The macro-mesoporous CeO₂ showed some typical features usually detected on this oxide, for example, the wide band at around 3500 cm⁻¹ together with the band at 1625 cm⁻¹ are assigned to the stretching and bending vibrations of the residual water molecules. The broad envelope of bands in the 1500–900 cm⁻¹ range is an indication of the presence of carbonate species [46]. In accordance with the literature, in fact, the appearance of carbonates is ascribed to the reaction of the surface CeO₂ oxygen with the atmospheric CO₂ [47]. In particular, the bands at around 986 and 862 cm⁻¹ are attributed to the formation of polydentate carbonates, whereas the strong band at around 1100 cm⁻¹, not present in the metal supported catalysts, could be due to bridged carbonates [46]. Finally, the band at around 700 cm⁻¹ is assigned to the O–Ce–O vibrations. Interestingly, with the addition of the metal species, some differences are detected in the “carbonate” zone (Figure 4b). Specifically, in both mono and bimetallic samples, two bands are present in the 1560–1470 cm⁻¹ (ν_{as} COO⁻) and 1370–1300 cm⁻¹ (ν_s COO⁻) ranges, which are assigned to the monodentate carbonate species [48], and which are absent in the bare CeO₂ sample. As reported in the literature, the value of the shift between these two bands ($\Delta\nu = \nu_{as}$ COO⁻ – ν_s COO⁻) gives an indication of the basicity of the oxygen involved in the monodentate carbonate formation: the higher the value of $\Delta\nu$, the lower the oxygen basicity (namely more covalent is the M–O bond) [48]. For the Au/CeO₂, the $\Delta\nu$ is equal to 144 cm⁻¹, a value that is lower than that of Ag/CeO₂ (190 cm⁻¹) and AuAg/CeO₂ (198 cm⁻¹, bands also less intense). Furthermore, the bands assigned to the polydentate carbonate are shifted and broader in all metals-loaded samples compared to the bare CeO₂, which are at 996 cm⁻¹ and 858 cm⁻¹ for Au/CeO₂, at 991 cm⁻¹ and 854 cm⁻¹ for Ag/CeO₂ and at 988 cm⁻¹ and 868 cm⁻¹ for AuAg/CeO₂ (bands more intense). These data show that the addition of metals on the macro-mesoporous CeO₂ lowers the basicity of CeO₂ oxygens, which makes the bimetallic AuAg/CeO₂ sample the least basic catalyst. This behavior has been connected to a rise of ceria oxygen storage capacity (OSC), which is advantageous for the oxidation reactions [32,49].

**Figure 4.** (a) Fourier Transform Infrared spectra of the investigated catalysts; (b) zoom on the “carbonate” zone.

2.2. Reducibility Properties

The Temperature Programmed Reduction in hydrogen (H_2 -TPR) measurements (Figure 5) were carried out to inspect the reducibility properties of the as-synthesized powders. The macro-mesoporous CeO_2 support displayed one peak in the range of 500–600 °C. This feature is ascribed to the surface oxygen's reduction [31,32], whereas the reduction of ceria bulk oxygen is accounted to occur at $T > 700$ °C [50,51] and does not appear in our TPR profiles. Both Au and Ag monometallic catalysts exhibited one single peak, centered at 158 °C for Au/ CeO_2 and at 174 °C for Ag/ CeO_2 , attributed to the reduction of the surface oxygen of cerium oxide, which appears at much lower temperatures on the metal loaded samples. The detected shifts are a proof of the existence of an interaction between Au or Ag with CeO_2 , which favors a high mobility/reducibility of the ceria lattice oxygen by undermining the Ce–O bonds [31,32,52]. The lower temperature of reduction measured on the Au/ CeO_2 catalyst with respect to Ag/ CeO_2 , in accordance with the literature data, evidenced a higher interaction of Au with ceria [53]. Interestingly, with the bimetallic Au-Ag sample, the maximum of the reduction peak was further shifted at lower temperature (102 °C) compared to the monometallic ones, highlighting the highest reducibility of ceria surface oxygen, with the establishment of a strong interaction between Au-Ag and the macro-mesoporous CeO_2 support.

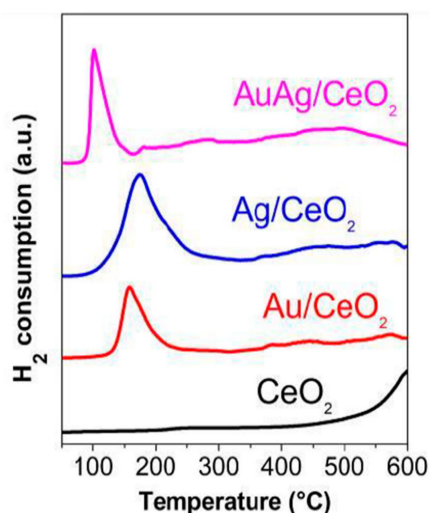


Figure 5. H_2 -Temperature Programmed Reduction curves of the investigated catalysts.

2.3. Surface Properties

The surface properties and the surface composition of the analyzed catalysts were determined by X-ray Photoelectron Spectroscopy (XPS) [54,55]. Figure 6a shows the XPS spectrum of the AuAg/ CeO_2 sample in the Au 4f binding energy region. The Au 4f_{7/2,5/2} spin-orbit components lie at 83.6 and 87.3 eV (3.7 eV spin-orbit coupling), respectively, pointing to the attendance of the Au⁰ state, whose 4f_{7/2} levels are reported to be at 84.0 eV [56–59]. These binding energies match with those measured for the Au/ CeO_2 sample (Figure S3a). However, the Au 4f levels of the bimetallic catalyst are broader with respect to those observed for the monometallic system (vide infra).

The XPS spectrum of the Ag/ CeO_2 sample shows the Ag 3d_{5/2,3/2} spin-orbit signals at 367.8 and 373.7 eV (Figure S3b), in tune with the presence of the Ag⁰ states [33,44]. Figure 6b illustrates the XPS spectrum of the bimetallic AuAg/ CeO_2 sample in the Ag 3d binding energy region. The Ag 3d_{5/2,3/2} spin-orbit components lie at 368.2 and 374.1 (5.9 eV spin-orbit coupling), respectively, and at 0.4 eV at higher binding energies than those observed for the monometallic Ag/ CeO_2 catalyst. This experimental observation indicates the interaction between silver and gold nanoparticles. In fact, the observed higher binding energies of the Ag states are due to the higher electronegativity of gold (2.54) with respect to that of both cerium (1.12) and silver (1.93). In addition, this evidence is also substantiated by the above-mentioned Au 4f_{7/2,5/2} spin-orbit energies (83.6 and 87.3 eV), which are 0.4 eV lower

than those usually expected for Au^0 state because of the electron withdrawing capability of gold. As a whole, the XPS results are in tune with the formation of (conjugated) interacting Au-Ag NPs in the bimetallic AuAg/CeO₂ sample.

Concerning the Ce 3d levels for AuAg/CeO₂, XPS shows a large envelope consisting of six different peaks (Figure 6c). Those at 882.1, 888.4 and 898.2 eV are due to the Ce 3d_{5/2} states and those at 900.5, 907.2 and 916.4 eV are due to the Ce 3d_{3/2} states. On the basis of previous literature reports, the first two peaks at 882.1 and 888.4 eV can be safely assigned to the two mixed 3d⁹4f²(O 2p⁴) and 3d⁹4f¹(O 2p⁵) Ce⁴⁺ electronic states, and the peak at 898.2 eV belongs to the 3d⁹4f⁰(O 2p⁶) Ce⁴⁺ state. The remaining peaks at 900.5, 907.2 and 916.4 eV are the related 3d_{3/2} spin-orbit signals of the same electronic states. Moreover, there is no evidence of any 3d⁹4f¹(O 2p⁶) Ce³⁺ final state, thus excluding the cerium lower oxidation state [12,60]. These XPS values are almost equivalent to those observed for the Au/CeO₂ sample. The spectra of the Ag/CeO₂ sample in the Ce 3d binding energy interval shows the same cerium components at ~0.4 eV lower binding energies, and this is due to the absence of the electron withdrawing power of gold in the Ag/CeO₂ catalyst.

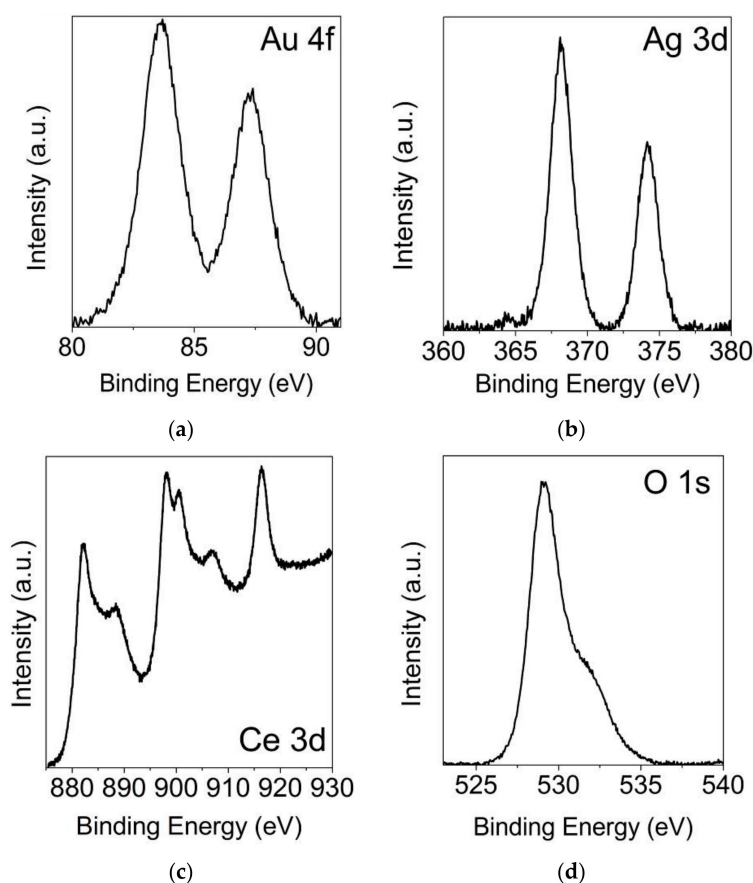


Figure 6. Al-K α excited X-ray Photoelectron Spectroscopy of the AuAg/CeO₂ sample in the Au 4f binding energy region (a), in the Ag 3d binding energy region (b), in the Ce 3d binding energy region (c) and in O 1s binding energy region (d).

Finally, Figure 6d shows the O 1s spectrum for the Au-Ag/CeO₂ sample, which consists of two peaks at 529.1 and 531.6 eV, respectively [12,61,62]. The first oxygen signal refers to the CeO₂ lattice oxygen (O²⁻), while the second signal belongs to the chemisorbed OH⁻ groups [12,60]. These XPS values are almost equivalent with those observed for the Au/CeO₂ and Ag/CeO₂ samples. The surface compositions of the three investigated catalysts were determined on the basis of XPS atomic concentration analysis. The Au/Ce and Ag/Ce are 0.04 and 0.05 for Au/CeO₂ and Ag/CeO₂, respectively, while in the AuAg/CeO₂ sample the Au/Ag surface ratio is 1, with (Au + Ag)/Ce = 0.06.

These values are in line with the nominal molar ratio of the analyzed catalysts. Moreover, the Energy Dispersive X-ray analysis (EDX) of the AuAg/CeO₂ sample (Figure S1c) stated a similar ratio ((Au + Ag)/Ce = 0.08) to that measured through XPS.

2.4. Catalytic Activity on the CO-PROX Reaction

The catalytic activity results of the as-synthesized mono and bimetallic samples supported on macro-mesoporous CeO₂ are illustrated in the (Figure 7). Considering the CO conversion (Figure 7a), it is possible to note that the bimetallic Au-Ag sample is the best performing catalyst, reaching the 94% of conversion at 80 °C with a catalytic activity higher than the sum of the activities of the corresponding monometallic catalysts. This catalytic behavior can be related to the establishment of a strong interaction between the two metals and the support. The monometallic gold sample showed a CO maximum conversion of 64% at 80 °C, whereas the Ag/CeO₂ is the less active catalyst (CO maximum conversion of 26% at 140 °C). The O₂ conversion (Figure 7b) increased with the temperature, reaching the 100% conversion at a temperature higher than 120 °C. Interestingly, in terms of O₂ conversion, the AuAg/CeO₂ sample is the least active of the catalysts.

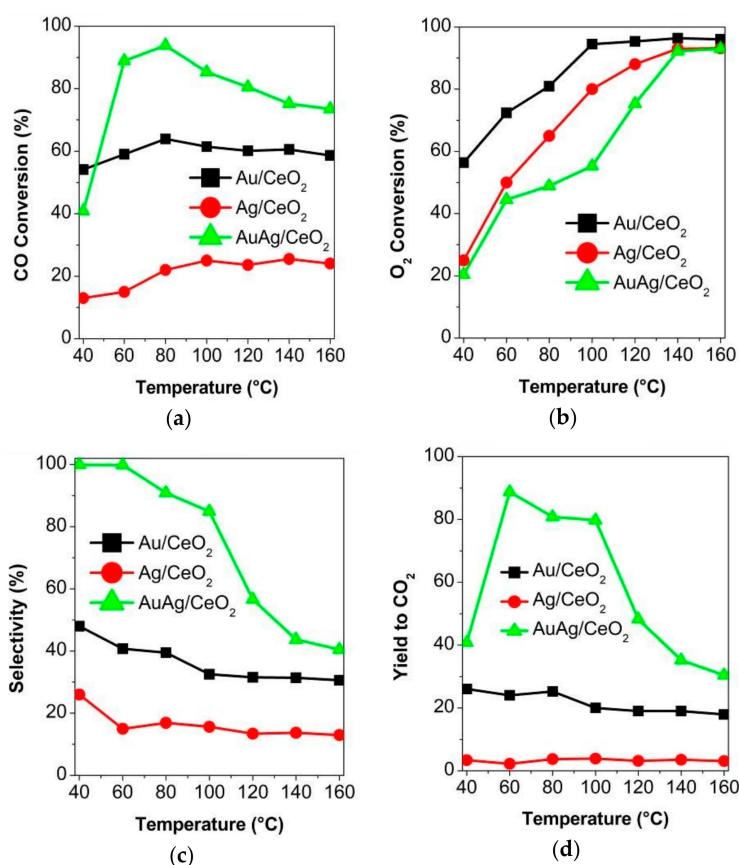


Figure 7. Catalytic activity on the CO-Preferential oxidation reaction: (a) conversion of CO; (b) conversion of O₂; (c) selectivity to CO₂; (d) yield to CO₂.

For a possible industrial application, selectivity towards the CO oxidation is a fundamental parameter (Figure 7c). As reported in the literature, the selectivity decreased on increasing the reaction temperature [31,63]. Indeed, the activation energy of the H₂ oxidation was higher than that of the CO oxidation; therefore, the former reaction is favored at a high temperature, thus explaining the drop of the CO selectivity. Noteworthy, the occurrence of the reverse water gas shift reaction (RWGS) can not be excluded. Nevertheless, it was reported that the RWGS reaction takes place at a temperature higher than those investigated in this work [31,32,64]. The AuAg/CeO₂ is the best selective catalyst, with selectivity values that remain around the 100–85% at low temperatures (40–100 °C), about two times

higher than Au/CeO₂ in the same temperature range (48–33%) and much higher than the Ag/CeO₂ catalyst (selectivity below the 30%). As a consequence, regarding the yields to CO₂, the bimetallic sample showed the highest values, with a maximum of 89% at 60 °C. These data corroborate as the Au-Ag system is the best one compared to monometallic gold (maximum of CO₂ yield of 25% at 80 °C) and silver (maximum of CO₂ yield of 4% at 100 °C). It is important to highlight that the higher activity of the AuAg/CeO₂ sample is not related to the amount of metals present on the catalyst, which is the sum of the nominal wt% (0.5% Au-0.5% Ag) equal to that of the monometallic materials (1 wt%). In all the experiments, no methane was detected, and no relevant CO and O₂ conversion was measured on the bare macro-mesoporous CeO₂ support.

3. Discussion

The above reported data underline the establishment of an effective interaction between gold-silver and the macro-mesoporous CeO₂, which allows us to obtain good results in the CO-PROX reaction. As reported in the literature [12,65], especially when a reducible oxide (as CeO₂) is employed as support, the activation of oxygen is a crucial step in view of the subsequent reaction with the CO molecules. The oxygen involved in the reaction can be activated on the metal/CeO₂ boundary and/or the surface oxygen of CeO₂. Anyway, it is important to remind that the oxygen can react both with CO and H₂, and then the ideal catalyst should be able to preferentially direct the reaction towards the CO oxidation, therefore providing a good selectivity and CO₂ yield. As confirmed by the TPR measurements, the high mobility, i.e., reducibility, of the surface oxygen of the cerium oxide can be further boosted by the addition of gold and silver on its surface [12,31,32,52]. This feature is beneficial for the oxidation reaction and particularly for the CO-PROX, which increases the CO₂ production. The reaction mechanism on ceria-supported catalyst follows, as reported, a Mars–Van Krevelen (MvK) pathway [32,66,67]. The first step consists of the chemisorption of the reagent molecules (CO, H₂ and O₂) on the surface of the sample, followed by the desorption of the reaction products (carbon dioxide and water), which generate oxygen vacancies in the lattice of cerium oxide (CeO₂ → Ce₂O₃). Then, these vacancies are filled by oxygen from the gas-phase (Ce₂O₃ + 1/2O₂ → 2CeO₂) closing in this way, the redox cycle of CeO₂. Considering this reaction mechanism, it is clear that the reactivity/reducibility of the ceria, which reflects the mobility of its surface oxygen [12,31,32,68], is a key parameter that is directly implied in the CO-PROX reaction. The oxygen, indeed, interacts with the carbon monoxide at the metal/CeO₂ interface to produce carbon dioxide. As confirmed by the TPR measurements, the reducibility of the involved oxygen of the cerium oxide is increased by the addition of the noble metals, and in particular, the highest reducibility (and therefore mobility) was detected with the addition of both gold and silver. Moreover, the high dispersion of metals on the macro-mesoporous channels of the ceria support allows further boosting of the reducibility, i.e., the reactivity of the surface ceria oxygen. As a consequence, the Au-Ag bimetallic catalyst exhibited the highest CO₂ selectivity and yield at low temperatures (60–100 °C), matching perfectly the operation temperature range of the PEMFC. These results can be also related to the lowest basicity of the AuAg/CeO₂ sites compared to the monometallic samples, as pointed out by FTIR analysis. This feature is useful for the oxidation reactions and increases the oxygen storage ability of CeO₂ [32,49]. Moreover, the occurrence of a conjugated interaction between gold and silver was further confirmed by XPS analysis, pointing to an electron transfer from silver to gold. These electrons can subsequently move to the cerium oxide support, further enhancing the reducibility/mobility of the CeO₂ oxygen. As reported in the literature, indeed, the modification of the electron properties of the other metal is a typical feature of the gold-based bimetallic systems, due to the high electronegativity of gold, [69,70].

The catalytic behavior of the AuAg/CeO₂ sample towards the preferential oxidation of CO in H₂-rich streams and in the PEMFC temperature operating window (60–100 °C) is in line, or even better than that of other mono and bimetallic samples supported on the macro/mesoporous CeO₂ (Table 2 with associated references). We also found that the performances of AuAg/CeO₂ were much higher than the corresponding AuAg samples supported on commercial SiO₂ and Al₂O₃ (Figure S4), thus

confirming the key role of the support. The peculiar structure, due to the interconnected pores of the ceria, favors a quick mass transfer and a high dispersion of the metal active species, which are fundamental features to raise the performance of AuAg/CeO₂.

Table 2. CO-PROX activity of various mono and bimetallic catalysts reported on in the literature in comparison to the AuAg/CeO₂ sample investigated in this work.

Sample	Metal Loading	Support	Gas Mixture (vol.%)	CO Conversion (%)	CO ₂ Selectivity (%)	Ref.
AuAg/CeO ₂	0.5%–0.5% wt	Macro-mesoporous CeO ₂	1 CO, 1 O ₂ , 88 H ₂ , rest He	89 (60 °C) 85 (100 °C)	100 (60 °C) 85 (100 °C)	this work
AuPt/CeO ₂	0.5%–0.5% wt	Macro-mesoporous CeO ₂	1 CO, 1 O ₂ , 50 H ₂ , rest He	65 (60 °C) 85(100 °C)	100 (60 °C) 75 (100 °C)	[39]
Cu _x Ce _{1-x} -BTC MOFs	Cu 0.7/Ce0.7 mol	BTC MOFs	1 CO, 1 O ₂ , 50 H ₂ , rest N ₂	40 (60 °C) 96(100 °C)	70 (60 °C) 90 (100 °C)	[71]
Au/CeO ₂ -Fe ₂ O ₃	3% wt	Mesoporous CeO ₂ -Fe ₂ O ₃	1 CO, 1.5 O ₂ , 10 CO ₂ , 10% H ₂ O, 50% H ₂ rest He	80 (60 °C) 80 (100 °C)	35 (60 °C) 30 (100 °C)	[38]
Cu–Ce–O	14% CuO mol	Mesoporous CeO ₂	1 CO, 1 O ₂ , 50 H ₂ , rest N ₂	30 (60 °C) 60 (100 °C)	100 (60 °C) 90 (100 °C)	[72]
Co/CeO ₂	30% wt	Mesoporous CeO ₂	1 CO, 1 O ₂ , 50 H ₂ , rest Ar	10 (60 °C) 20 (100 °C)	100 (60 °C) 100 (100 °C)	[73]
CuO/CeO ₂	not reported	Macro-mesoporous CeO ₂	1 CO, 1 O ₂ , 50 H ₂ , rest N ₂	10 (60 °C) 60 (100 °C)	100 (60 °C) 100 (100 °C)	[74]

For a possible scale-up utilization of the best performing catalyst, in our case AuAg/CeO₂, it was interesting to investigate the catalytic stability of the sample in the presence of water and CO₂ (Figure 8). During 8 h of time on stream at 100 °C, the AuAg/CeO₂ exhibited no substantial decrease of the CO conversion in the presence of CO₂, whereas a slight increase was verified in the presence of water (Figure 8a). This behavior is in accordance with the literature and was ascribed to the promotion of the water gas shift reaction in the presence of water ($\text{CO} + \text{H}_2\text{O} \rightleftharpoons \text{CO}_2 + \text{H}_2$) and/or to the decomposition of carbonate species [7,75,76]. The fully reversible slight deactivation in the presence of carbon dioxide was reasonably attributed to the competitive adsorption process on the surface of the catalyst between CO₂, CO and H₂, and/or to the formation of carbonates, which can seal the catalyst active sites [7,75,76]. Interestingly, the effects of H₂O and CO₂ are attenuated at low temperature, as they can be seen in the Figure 8b. Furthermore, the catalytic performance of AuAg/CeO₂ versus temperature in the presence of CO₂ or water vapor (Figure S5) showed only slight variations in the activity compared to the results obtained adopting the used PROX gas mixture.

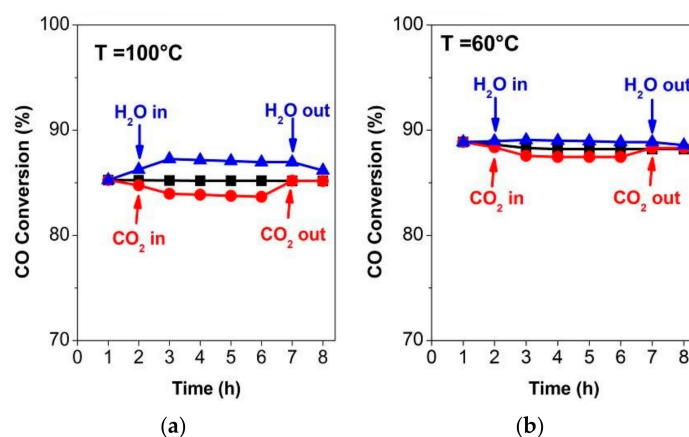


Figure 8. CO conversion versus time of stream over the AuAg/CeO₂ catalyst under diverse conditions: gas mixture (black line), water addition (blue line) and carbon dioxide addition (red line). (a) Reaction temperature of 100 °C, and (b) reaction temperature of 60 °C.

4. Materials and Methods

4.1. Catalysts Synthesis

Macro-mesoporous CeO₂ was prepared using polystyrene spheres as a template following the reported procedure for the synthesis of inverse opal materials [41,77,78]. The spheres were produced through a free-surfactant emulsion polymerization. The styrene (Sigma-Aldrich, Buchs, Switzerland) was washed with a solution of NaOH (1 M, Fluka, Buchs, Switzerland) to remove the 4-*tert*-butylcatechol stabilizer. Afterwards, the resulting mixture was stirred under argon atmosphere and heated to 70 °C. To start the polymerization, potassium persulfate K₂S₂O₈ (0.16 g, Sigma-Aldrich, Buchs, Switzerland) was added. After 5 h, the polymerization was stopped and the flask was opened and cooled at the room temperature. The obtained polystyrene dispersion in water was self-assembled by drying at 40 °C for 5 days. Finally, the as-synthesized spheres (diameter of about 300 nm) were impregnated with a cerium nitrate hexahydrate (Fluka, Buchs, Switzerland) solution and dried at 40 °C overnight. The removal of the polystyrene spheres and the crystallization of CeO₂ with a macro-mesoporous structure were achieved by calcination at 450 °C for 5 h.

The deposition-precipitation was employed for the preparation of the mono and bimetallic samples. In particular, the water solutions of the metal salt precursors, namely tetrachloroauric (III) acid (Sigma-Aldrich, Buchs Switzerland) for gold, and silver nitrate (Sigma-Aldrich, Buchs, Switzerland) for silver, were stabilized at pH = 8 through 0.1 M potassium hydroxide (Fluka, Buchs, Switzerland). Afterwards, the macro-mesoporous ceria was dipped into the solution under stirring. The resultant slurry was stirred at 70 °C for 3 h, and then digested for 24 h. Finally, it was filtered and washed until the removal of the nitrates and chlorides, and then it was dried at 110 °C. The weight % of metals was 1 for the monometallic samples, and 0.5 Au and 0.5 Ag for the bimetallic one.

4.2. Catalysts Characterization

SEM was performed with Jeol JSM-7500F (JEOL Europe SAS, Allée de Giverny, France).

TEM was carried out with JEOL JEM 2100F (JEOL Europe SAS, Allée de Giverny, France) operating at 200 kV and utilizing an INCA Energy Oxford solid state detector (Oxford Instruments NanoAnalysis & Asylum Research, Oxford, UK) for EDX determination.

BET surface area and BJH pore size distribution were determined through nitrogen physisorption by a Sorptomatic series 1990 instrument (Thermo Quest, Milano, Italy). All the analyzed catalysts were outgassed at 120 °C overnight.

FTIR analyses in the 4000–700 cm⁻¹ region were attained using FT-IR System 2000 (Perkin-Elmer, Waltham, MA, USA).

H₂-TPR measurements were achieved heating, with a ramp of ten degrees per minute, 0.05 g of the powder samples in a flow of hydrogen (5 vol.%) balanced with argon, employing a thermal conductivity detector (according to the procedure reported in ref. [31]).

XRD measurements were carried out with an AXSD5005 X-ray diffractometer (Bruker, Karlsruhe, Germany), employing the Cu K α radiation and the JCPDS software (Bruker, Diffrac. Suite™ Software package, Karlsruhe, Germany) in order to compare the detected peaks with the standard ones.

XPS spectra were measured at a 45° take-off angle relative to the surface plane, with a PHI 5600 Multi Technique System (energy resolution ≤ 0.5 eV, Chanhassen, MN, USA). The powder catalysts were excited with Al K α X-ray radiation. Spectra calibration was obtained fixing the C 1s signal at 285.0 eV. Further details regarding the data processing were reported in the references [12,79,80]). For the XPS measurements the samples were pre-treated, with the same conditions utilized for the catalytic tests (see next paragraph).

4.3. CO-PROX Reaction in H₂ Rich Steam

The preferential oxidation of CO was carried out in a continuous flow gas-phase reactor (P = 1 atm) using 0.05 g of the catalyst (80–140 mesh) and 0.45 g of inert glass powder. A measure of 80 mL/min of

the gas mixture (CO 1 vol.%; O₂ 1 vol.%; He 10 vol.% and the rest H₂) and 3.92×10^{-2} mol_{CO}/h·g_{cat} gas hour space velocity were chosen. The catalytic stability tests were performed in the presence of water vapor (2 vol.%) or carbon dioxide (5 vol.%). The reaction products were determined through gas-chromatography using the same apparatus and procedures reported in the references [7,12,31,32]. The catalysts were pre-treated before reaction by calcination at 200 °C for one hour, and then the reduction in hydrogen at 200 °C for one hour.

5. Conclusions

In this work, mono and bimetallic gold-based catalysts supported on macro-mesoporous CeO₂ were successfully synthesized. The bimetallic AuAg/CeO₂ sample exhibited the best performance toward the CO-PROX in an H₂-rich stream. The high porosity of the ceria support favored the dispersion of the metals, and the effective interaction between gold and silver enhanced the mobility/reducibility of CeO₂ surface oxygen. The good stability as a function of time, and the high performance in the PEMFC range (60–100 °C), allowed us to consider the AuAg/macro-mesoporous CeO₂ system as a promising candidate for a possible scale-up application in the field of H₂ purification by CO-PROX reaction for the hydrogen exploitation in the PEMFC.

Supplementary Materials: The following are available online at <http://www.mdpi.com/2073-4344/10/1/49/s1>: Figure S1a,b: HRTEM of Ag/CeO₂ and AuAg/CeO₂ samples, Figure S1c: EDX map of the AuAg/CeO₂ catalyst, Figure S2: XRD patterns of all the analyzed samples, Figure S3: XPS images of Au/CeO₂ sample in the Au 4f binding energy region and of Ag/CeO₂ sample in the Ag 3d region, Figure S4: Comparison of the CO₂ yields obtained with AuAg/CeO₂, AuAg/SiO₂ and AuAg/Al₂O₃ catalysts and Figure S5: Comparison of the catalytic activity in function of temperature of the AuAg/CeO₂ sample in the presence of CO₂ or water vapor.

Author Contributions: R.F. conceived the idea of writing the manuscript, synthesized the catalysts, designed and carried out the PROX tests and TPR, FTIR and surface area determinations. A.G. and L.S. executed and commented XPS characterization. S.S. supervised the work and edited the manuscript. All authors have read and agreed to the published version of the manuscript.

Funding: R.F. thanks the PON project “AIM” founded by the European Social Found (ESF) CUP: E66C18001220005 for the financial support.

Acknowledgments: We thank Bao-Lian Su, director of Laboratory of Inorganic Materials Chemistry (CMI), University of Namur (Belgium), for the SEM, TEM and EDX measurements and G.G. Condorelli, University of Catania, to have performed the XRD analyses.

Conflicts of Interest: The authors declare no conflict of interest.

References

1. Wong, C.Y.; Wong, W.Y.; Ramya, K.; Khalid, M.; Loh, K.S.; Daud, W.R.W.; Lim, K.L.; Walvekar, R.; Kadhum, A.A.H. Additives in proton exchange membranes for low- and high-temperature fuel cell applications: A review. *Int. J. Hydrog. Energy* **2019**, *44*, 6116–6135. [[CrossRef](#)]
2. Wang, Y.; Leung, D.Y.C.; Xuan, J.; Wang, H. A review on unitized regenerative fuel cell technologies, part-A: Unitized regenerative proton exchange membrane fuel cells. *Renew. Sustain. Energy Rev.* **2016**, *65*, 961–977. [[CrossRef](#)]
3. Robledo, C.B.; Oldenbroek, V.; Abbruzzese, F.; van Wijk, A.J.M. Integrating a hydrogen fuel cell electric vehicle with vehicle-to-grid technology, photovoltaic power and a residential building. *Appl. Energy* **2018**, *215*, 615–629. [[CrossRef](#)]
4. Bizon, N.; Lopez-Guede, J.M.; Kurt, E.; Thounthong, P.; Mazare, A.G.; Ionescu, L.M.; Iana, G. Hydrogen economy of the fuel cell hybrid power system optimized by air flow control to mitigate the effect of the uncertainty about available renewable power and load dynamics. *Energy Convers. Manag.* **2019**, *179*, 152–165. [[CrossRef](#)]
5. Shamsuzzoha, M.; Son, I.H. Promotion of Pt/γ-Al₂O₃ by new pretreatment for low-temperature preferential oxidation of CO in H₂ for PEM fuel cells. *J. Catal.* **2002**, *210*, 460–465.
6. Yoshida, Y.; Izumi, Y. Recent Advances in the Preferential Thermal-/Photo-Oxidation of Carbon Monoxide: Noble Versus Inexpensive Metals and Their Reaction Mechanisms. *Catal. Surv. Asia* **2016**, *20*, 141–166. [[CrossRef](#)]

7. Scirè, S.; Fiorenza, R.; Gulino, A.; Cristaldi, A.; Riccobene, P.M. Selective oxidation of CO in H₂-rich stream over ZSM5 zeolites supported Ru catalysts: An investigation on the role of the support and the Ru particle size. *Appl. Catal. A Gen.* **2016**, *520*, 82–91. [CrossRef]
8. Yuranov, I.; Autissier, N.; Sordakis, K.; Dalebrook, A.F.; Grasmann, M.; Orava, V.; Cendula, P.; Gubler, L.; Laurenczy, G. Heterogeneous Catalytic Reactor for Hydrogen Production from Formic Acid and Its Use in Polymer Electrolyte Fuel Cells. *ACS Sustain. Chem. Eng.* **2018**, *6*, 6635–6643. [CrossRef]
9. Cao, L.; Liu, W.; Luo, Q.; Yin, R.; Wang, B.; Weissenrieder, J.; Soldemo, M.; Yan, H.; Lin, Y.; Sun, Z.; et al. Atomically dispersed iron hydroxide anchored on Pt for preferential oxidation of CO in H₂. *Nature* **2019**, *565*, 631–635. [CrossRef]
10. Navlani-García, M.; Miguel-García, I.; Berenguer-Murcia, Á.; Lozano-Castelló, D.; Cazorla-Amorós, D.; Yamashita, H. Pd/zeolite-based catalysts for the preferential CO oxidation reaction: Ion-exchange, Si/Al and structure effect. *Catal. Sci. Technol.* **2016**, *6*, 2623–2632. [CrossRef]
11. Di, L.; Wu, G.; Dai, W.; Guan, N.; Li, L. Ru/TiO₂ for the preferential oxidation of CO in H₂-rich stream: Effects of catalyst pre-treatments and reconstruction of Ru sites. *Fuel* **2015**, *143*, 318–326. [CrossRef]
12. Fiorenza, R.; Spitaleri, L.; Gulino, A.; Scirè, S. Ru–Pd Bimetallic Catalysts Supported on CeO₂–MnO_x Oxides as Efficient Systems for H₂ Purification through CO Preferential Oxidation. *Catalysts* **2018**, *8*, 203. [CrossRef]
13. Martínez, T.; Leidy, M.; Laguna, O.H.; López-Cartes, C.; Centeno, M.A. Synthesis and characterization of Rh/MnO₂–CeO₂/Al₂O₃ catalysts for CO-PrOx reaction. *Mol. Catal.* **2017**, *440*, 9–18. [CrossRef]
14. Cecilia, J.; Arango-Díaz, A.; Marrero-Jerez, J.; Núñez, P.; Moretti, E.; Storaro, L.; Rodríguez-Castellón, E. Catalytic Behaviour of CuO–CeO₂ Systems Prepared by Different Synthetic Methodologies in the CO-PROX Reaction under CO₂–H₂O Feed Stream. *Catalysts* **2017**, *7*, 160. [CrossRef]
15. Martínez-Arias, A.; Gamarra, D.; Hungría, A.; Fernández-García, M.; Munuera, G.; Hornés, A.; Bera, P.; Conesa, J.; Cámara, A. Characterization of Active Sites/Entities and Redox/Catalytic Correlations in Copper-Ceria-Based Catalysts for Preferential Oxidation of CO in H₂-Rich Streams. *Catalysts* **2013**, *3*, 378–400. [CrossRef]
16. Xu, C.; Li, S.; Zhang, Y.; Li, Y.; Zhou, J.; Qin, G. Synthesis of CuOx–CeO₂ catalyst with high-density interfaces for selective oxidation of CO in H₂-rich stream. *Int. J. Hydrog. Energy* **2019**, *44*, 4156–4166. [CrossRef]
17. Di Benedetto, A.; Landi, G.; Lisi, L. Improved CO-PROX Performance of CuO/CeO₂ Catalysts by Using Nanometric Ceria as Support. *Catalysts* **2018**, *8*, 209. [CrossRef]
18. Guo, X.; Zhou, R. Identification of the nano/micro structure of CeO₂ (rod) and the essential role of interfacial copper-ceria interaction in CuCe (rod) for selective oxidation of CO in H₂-rich streams. *J. Power Sources* **2017**, *361*, 39–53. [CrossRef]
19. Konsolakis, M. The role of Copper–Ceria interactions in catalysis science: Recent theoretical and experimental advances. *Appl. Catal. B Environ.* **2016**, *198*, 49–66. [CrossRef]
20. Aneggi, E.; Boaro, M.; De Leitenburg, C.; Dolcetti, G.; Trovarelli, A. Insights into the redox properties of ceria-based oxides and their implications in catalysis. *J. Alloy. Compd.* **2006**, *408–412*, 1096–1102. [CrossRef]
21. Scirè, S.; Palmisano, L. *Cerium Oxide (CeO₂): Synthesis, Properties and Applications, a Volume in Metal Oxides Series*; Elsevier: Amsterdam, The Netherlands, 2020; ISBN 978-0-12-815661-2. Available online: <https://doi.org/10.1016/C2017-0-02724-6> (accessed on 27 December 2019).
22. Hartadi, Y.; Behm, R.; Widmann, D. Competition of CO and H₂ for Active Oxygen Species during the Preferential CO Oxidation (PROX) on Au/TiO₂ Catalysts. *Catalysts* **2016**, *6*, 21. [CrossRef]
23. Leal, G.B.; Ciotti, L.; Watacabe, B.N.; Loureiro da Silva, D.C.; Antoniassi, R.M.; Silva, J.C.M.; Linardi, M.; Giudici, R.; Vaz, J.M.; Spinacé, E.V. Preparation of Au/TiO₂ by a facile method at room temperature for the CO preferential oxidation reaction. *Catal. Commun.* **2018**, *116*, 38–42. [CrossRef]
24. Moreno, M.S.; López, E.; Adrover, M.E.; Divins, N.J.; Llorca, J. CO-PrOx over nano-Au/TiO₂: Monolithic catalyst performance and empirical kinetic model fitting. *Int. J. Hydrog. Energy* **2016**, *41*, 22043–22054. [CrossRef]
25. Lakshmanan, P.; Park, E. Preferential CO Oxidation in H₂ over Au/La₂O₃/Al₂O₃ Catalysts: The Effect of the Catalyst Reduction Method. *Catalysts* **2018**, *8*, 183. [CrossRef]
26. Centeno, M.; Ramírez Reina, T.; Ivanova, S.; Laguna, O.; Odriozola, J. Au/CeO₂ Catalysts: Structure and CO Oxidation Activity. *Catalysts* **2016**, *6*, 158. [CrossRef]
27. Soler, L.; Casanovas, A.; Urrich, A.; Angurell, I.; Llorca, J. CO oxidation and COPrOx over preformed Au nanoparticles supported over nanoshaped CeO₂. *Appl. Catal. B Environ.* **2016**, *197*, 47–55. [CrossRef]

28. Qiao, B.; Liu, J.; Wang, Y.G.; Lin, Q.; Liu, X.; Wang, A.; Li, J.; Zhang, T.; Liu, J. Highly Efficient Catalysis of Preferential Oxidation of CO in H₂-Rich Stream by Gold Single-Atom Catalysts. *ACS Catal.* **2015**, *5*, 6249–6254. [[CrossRef](#)]
29. Li, X.; Fang, S.S.S.; Teo, J.; Foo, Y.L.; Borgna, A.; Lin, M.; Zhong, Z. Activation and deactivation of Au-Cu/SBA-15 catalyst for preferential oxidation of CO in H₂-Rich Gas. *ACS Catal.* **2012**, *2*, 360–369. [[CrossRef](#)]
30. Daté, M.; Okumura, M.; Tsubota, S.; Haruta, M. Vital role of moisture in the catalytic activity of supported gold nanoparticles. *Angew. Chem. Int. Ed.* **2004**, *43*, 2129–2132. [[CrossRef](#)]
31. Fiorenza, R.; Crisafulli, C.; Condorelli, G.G.; Lupo, F.; Scirè, S. Au-Ag/CeO₂ and Au-Cu/CeO₂ Catalysts for Volatile Organic Compounds Oxidation and CO Preferential Oxidation. *Catal. Lett.* **2015**, *145*, 1691–1702. [[CrossRef](#)]
32. Fiorenza, R.; Crisafulli, C.; Scirè, S. H₂ purification through preferential oxidation of CO over ceria supported bimetallic Au-based catalysts. *Int. J. Hydrog. Energy* **2016**, *41*, 19390–19398. [[CrossRef](#)]
33. Sasirekha, N.; Sangeetha, P.; Chen, Y.W. Bimetallic Au-Ag/CeO₂ catalysts for preferential oxidation of CO in hydrogen-rich stream: Effect of calcination temperature. *J. Phys. Chem. C* **2014**, *118*, 15226–15233. [[CrossRef](#)]
34. Yang, H.; Liu, W.; Wang, Z.; Sun, G. The Synthesis of SiO₂@AuAg@CeO₂ Sandwich Structures with Enhanced Catalytic Performance Towards CO Oxidation. *ChemistrySelect* **2019**, *4*, 9688–9695. [[CrossRef](#)]
35. Monyanon, S.; Pongstabodee, S.; Luengnaruemitchai, A. Catalytic activity of Pt-Au/CeO₂ catalyst for the preferential oxidation of CO in H₂-rich stream. *J. Power Sources* **2006**, *163*, 547–554. [[CrossRef](#)]
36. Li, S.; Zhu, H.; Qin, Z.; Zhang, Y.; Wang, G.; Wu, Z.; Fan, W.; Wang, J. Catalytic Performance of Gold Supported on Mn, Fe and Ni Doped Ceria in the Preferential Oxidation of CO in H₂-Rich Stream. *Catalysts* **2018**, *8*, 469. [[CrossRef](#)]
37. Cámara, A.L.; Corberán, V.C.; Barrio, L.; Zhou, G.; Si, R.; Hanson, J.C.; Monte, M.; Conesa, J.C.; Rodriguez, J.A.; Martínez-Arias, A. Improving the CO-PROX performance of inverse CeO₂/CuO catalysts: Doping of the CuO component with Zn. *J. Phys. Chem. C* **2014**, *118*, 9030–9041. [[CrossRef](#)]
38. Reina, T.R.; Ivanova, S.; Idakiev, V.; Tabakova, T.; Centeno, M.A.; Deng, Q.F.; Yuan, Z.Y.; Odriozola, J.A. Nanogold mesoporous iron promoted ceria catalysts for total and preferential CO oxidation reactions. *J. Mol. Catal. A Chem.* **2016**, *414*, 62–71. [[CrossRef](#)]
39. Liu, Y.; Liu, B.; Liu, Y.; Wang, Q.; Hu, W.; Jing, P.; Liu, L.; Yu, S.; Zhang, J. Improvement of catalytic performance of preferential oxidation of CO in H₂-rich gases on three-dimensionally ordered macro- and meso-porous Pt-Au/CeO₂ catalysts. *Appl. Catal. B Environ.* **2013**, *142*, 615–625. [[CrossRef](#)]
40. Waterhouse, G.I.N.; Metson, J.B.; Idriss, H.; Sun-Waterhouse, D. Physical and optical properties of inverse opal CeO₂ photonic crystals. *Chem. Mater.* **2008**, *20*, 1183–1190. [[CrossRef](#)]
41. Fiorenza, R.; Bellardita, M.; Barakat, T.; Scirè, S.; Palmisano, L. Visible light photocatalytic activity of macro-mesoporous TiO₂-CeO₂ inverse opals. *J. Photochem. Photobiol. A Chem.* **2018**, *352*, 25–34. [[CrossRef](#)]
42. Casillas, D.C.; Wilkinson, D.C.; Stephen, C.L.; Ignatowich, M.J.; Haile, S.M.; Dunn, B.S. High-temperature structural stability of ceria-based inverse opals. *J. Am. Ceram. Soc.* **2017**, *100*, 2659–2668. [[CrossRef](#)]
43. Liu, X.; Wang, A.; Zhang, T.; Su, D.S.; Mou, C.Y. Au-Cu alloy nanoparticles supported on silica gel as catalyst for CO oxidation: Effects of Au/Cu ratios. *Catal. Today* **2011**, *160*, 103–108. [[CrossRef](#)]
44. Yang, H.; Deng, J.; Liu, Y.; Xie, S.; Wu, Z.; Dai, H. Preparation and catalytic performance of Ag, Au, Pd or Pt nanoparticles supported on 3DOM CeO₂-Al₂O₃ for toluene oxidation. *J. Mol. Catal. A Chem.* **2016**, *414*, 9–18. [[CrossRef](#)]
45. Sing, K.S.W.; Everet, D.H.; Haul, R.A.W. Reporting Physisorption Data for gas/solid system with Special Reference to the Determination of Surface Area and Porosity. *Pure Appl. Chem.* **1985**, *57*, 603–619. [[CrossRef](#)]
46. Natile, M.M.; Boccaletti, G.; Glisenti, A. Properties and reactivity of nanostructured CeO₂ powders: Comparison among two synthesis procedures. *Chem. Mater.* **2005**, *17*, 6272–6286. [[CrossRef](#)]
47. Rosynek, M.P.; Magnuson, D.T. Infrared study of carbon dioxide adsorption on lanthanum sesquioxide and trihydroxide. *J. Catal.* **1977**, *48*, 417–421. [[CrossRef](#)]
48. Davydov, A. *Molecular Spectroscopy of Oxide Catalyst Surfaces*; Sheppard, N.T., Ed.; JohnWiley & Sons Ltd.: Chichester, UK, 2003.
49. Tibiletti, D.; De Graaf, E.A.B.; Teh, S.P.; Rothenberg, G.; Farrusseng, D.; Mirodatos, C. Selective CO oxidation in the presence of hydrogen: Fast parallel screening and mechanistic studies on ceria-based catalysts. *J. Catal.* **2004**, *225*, 489–497. [[CrossRef](#)]

50. Tabakova, T.; Boccuzzi, F.; Manzoli, M.; Sobczak, J.W.; Idakiev, V.; Andreeva, D. A comparative study of nanosized IB/ceria catalysts for low-temperature water-gas shift reaction. *Appl. Catal. A Gen.* **2006**, *298*, 127–143. [[CrossRef](#)]
51. Trovarelli, A.; Dolcetti, G.; De Leitenburg, C.; Kašpar, J.; Finetti, P.; Santoni, A. Rh-CeO₂ interaction induced by high-temperature reduction. Characterization and catalytic behaviour in transient and continuous conditions. *J. Chem. Soc. Faraday Trans.* **1992**, *88*, 1311–1319. [[CrossRef](#)]
52. Scirè, S.; Riccobene, P.M.; Crisafulli, C. Ceria supported group IB metal catalysts for the combustion of volatile organic compounds and the preferential oxidation of CO. *Appl. Catal. B Environ.* **2010**, *101*, 109–117. [[CrossRef](#)]
53. Kundakovic, L.; Flytzani-Stephanopoulos, M. Reduction characteristics of copper oxide in cerium and zirconium oxide systems. *Appl. Catal. A Gen.* **1998**, *171*, 13–29. [[CrossRef](#)]
54. Gulino, A.; Mineo, P.; Scamporrino, E.; Vitalini, D.; Fragalà, I. Spectroscopic and microscopic characterization and behavior of an optical pH meter based on a functional hybrid monolayer molecular system: Porphyrin molecules covalently assembled on a molecularly engineered silica surface. *Chem. Mater.* **2006**, *18*, 2404–2410. [[CrossRef](#)]
55. Gulino, A.; Gupta, T.; Mineo, P.G.; Van Der Boom, M.E. Selective NO_x optical sensing with surface-confined osmium polypyridyl complexes. *Chem. Commun.* **2007**, *2*, 4878–4880. [[CrossRef](#)] [[PubMed](#)]
56. Spitaleri, L.; Nicotra, G.; Zimbone, M.; Contino, A.; Maccarrone, G.; Alberti, A.; Gulino, A. Fast and Efficient Sun Light Photocatalytic Activity of Au_ZnO Core-Shell Nanoparticles Prepared by a One-Pot Synthesis. *ACS Omega* **2019**, *4*, 15061–15066. [[CrossRef](#)] [[PubMed](#)]
57. Contino, A.; Maccarrone, G.; Spitaleri, L.; Torrisi, L.; Nicotra, G.; Gulino, A. One Pot Synthesis of Au_ZnO Core-Shell Nanoparticles Using a Zn Complex Acting as ZnO Precursor, Capping and Reducing Agent During the Formation of Au NPs. *Eur. J. Inorg. Chem.* **2018**, *2018*, 4659. [[CrossRef](#)]
58. Contino, A.; Maccarrone, G.; Fragalà, M.E.; Spitaleri, L.; Gulino, A. Conjugated Gold-Porphyrin Monolayers Assembled on Inorganic Surfaces. *Chem. A Eur. J.* **2017**, *23*, 14937–14943. [[CrossRef](#)]
59. Kaminker, R.; Lahav, M.; Altman, M.; Evmenenko, G.; Dutta, P.; Gulino, A.; Van Der Boom, M.E. Surface-confined core-shell structures based on gold nanoparticles and metal-organic networks. *Chem. Commun.* **2014**, *50*, 4635–4638. [[CrossRef](#)]
60. Ji, P.; Zhang, J.; Chen, F.; Anpo, M. Ordered mesoporous CeO₂ synthesized by nanocasting from cubic Ia3d mesoporous MCM-48 silica: Formation, characterization and photocatalytic activity. *J. Phys. Chem. C* **2008**, *112*, 17809–17813. [[CrossRef](#)]
61. Gulino, A.; Taverner, A.E.; Warren, S.; Harris, P.; Egdell, R.G. A photoemission study of Sb-doped TiO₂. *Surf. Sci.* **1994**, *315*, 351–361. [[CrossRef](#)]
62. Di Mauro, A.; Cantarella, M.; Nicotra, G.; Pellegrino, G.; Gulino, A.; Brundo, M.V.; Privitera, V.; Impellizzeri, G. Novel synthesis of ZnO/PMMA nanocomposites for photocatalytic applications. *Sci. Rep.* **2017**, *7*, 1–12. [[CrossRef](#)]
63. Scirè, S.; Crisafulli, C.; Minicò, S.; Condorelli, G.G.; Di Mauro, A. Selective oxidation of CO in H₂-rich stream over gold/iron oxide: An insight on the effect of catalyst pretreatment. *J. Mol. Catal. A Chem.* **2008**, *284*, 24–32. [[CrossRef](#)]
64. Mariño, F.; Descorme, C.; Duprez, D. Noble metal catalysts for the preferential oxidation of carbon monoxide in the presence of hydrogen (PROX). *Appl. Catal. B Environ.* **2004**, *54*, 59–66. [[CrossRef](#)]
65. Liu, K.; Wang, A.; Zhang, T. Recent advances in preferential oxidation of CO reaction over platinum group metal catalysts. *ACS Catal.* **2012**, *2*, 1165–1178. [[CrossRef](#)]
66. Laguna, O.H.; Centeno, M.A.; Arzamendi, G.; Gandía, L.M.; Romero-Sarria, F.; Odriozola, J.A. Iron-modified ceria and Au/ceria catalysts for total and preferential oxidation of CO (TOX and PROX). *Catal. Today* **2010**, *157*, 155–159. [[CrossRef](#)]
67. Doornkamp, C.; Ponec, V. The universal character of the Mars and Van Krevelen mechanism. *J. Mol. Catal. A Chem.* **2000**, *162*, 19–32. [[CrossRef](#)]
68. Campbell, C.T.; Peden, C.H.F. Oxygen vacancies and catalysis on ceria surfaces. *Science* **2005**, *309*, 713–714. [[CrossRef](#)]
69. Szumelda, T.; Drelinkiewicz, A.; Lalik, E.; Kosydar, R.; Duraczyńska, D.; Gurgul, J. Carbon-supported Pd₁₀₀-XAuX alloy nanoparticles for the electrocatalytic oxidation of formic acid: Influence of metal particles composition on activity enhancement. *Appl. Catal. B Environ.* **2018**, *221*, 393–405. [[CrossRef](#)]

70. Wang, A.Q.; Chang, C.M.; Mou, C.Y. Evolution of Catalytic Activity of Au-Ag Bimetallic Nanoparticles on Mesoporous Support for CO Oxidation. *J. Phys. Chem. B* **2005**, *109*, 18860–18867. [[CrossRef](#)]
71. Gong, X.; Wang, W.W.; Fu, X.P.; Wei, S.; Yu, W.Z.; Liu, B.; Jia, C.J.; Zhang, J. Metal-organic-framework derived controllable synthesis of mesoporous copper-cerium oxide composite catalysts for the preferential oxidation of carbon monoxide. *Fuel* **2018**, *229*, 217–226. [[CrossRef](#)]
72. Gu, D.; Jia, C.J.; Bongard, H.; Spliethoff, B.; Weidenthaler, C.; Schmidt, W.; Schüth, F. Ordered mesoporous Cu-Ce-O catalysts for CO preferential oxidation in H₂-rich gases: Influence of copper content and pretreatment conditions. *Appl. Catal. B Environ.* **2014**, *152*, 11–18. [[CrossRef](#)]
73. Yan, C.F.; Chen, H.; Hu, R.R.; Huang, S.; Luo, W.; Guo, C.; Li, M.; Li, W. Synthesis of mesoporous Co-Ce oxides catalysts by glycine-nitrate combustion approach for CO preferential oxidation reaction in excess H₂. *Int. J. Hydrog. Energy* **2014**, *39*, 18695–18701. [[CrossRef](#)]
74. Zhang, Y.; Liang, H.; Gao, X.Y.; Liu, Y. Three-dimensionally ordered macro-porous CuO-CeO₂ used for preferential oxidation of carbon monoxide in hydrogen-rich gases. *Catal. Commun.* **2009**, *10*, 1432–1436. [[CrossRef](#)]
75. Reina, T.R.; Ivanova, S.; Centeno, M.A.; Odriozola, J.A. Catalytic screening of Au/CeO₂-MO_x/Al₂O₃ catalysts (M = La, Ni, Cu, Fe, Cr, Y) in the CO-PrOx reaction. *Int. J. Hydrog. Energy* **2015**, *40*, 1782–1788. [[CrossRef](#)]
76. Liao, X.; Chu, W.; Dai, X.; Pitchon, V. Bimetallic Au-Cu supported on ceria for PROX reaction: Effects of Cu/Au atomic ratios and thermal pretreatments. *Appl. Catal. B Environ.* **2013**, *142–143*, 25–37. [[CrossRef](#)]
77. Fiorenza, R.; Bellardita, M.; Scirè, S.; Palmisano, L. Photocatalytic H₂ production over inverse opal TiO₂ catalysts. *Catal. Today* **2019**, *321*, 113–119. [[CrossRef](#)]
78. Fiorenza, R.; Scirè, S.; D'Urso, L.; Compagnini, G.; Bellardita, M.; Palmisano, L. Efficient H₂ production by photocatalytic water splitting under UV or solar light over variously modified TiO₂-based catalysts. *Int. J. Hydrog. Energy* **2019**, *44*, 14796–14807. [[CrossRef](#)]
79. Briggs, D.; Grant, J.T. *In Surface Analysis by Auger and X-ray Photoelectron Spectroscopy*; IM Publications: Chichester, UK; Surface Spectra Ltd.: Manchester, UK, 2003.
80. Gulino, A. Structural and electronic characterization of self-assembled molecular nanoarchitectures by X-ray photoelectron spectroscopy. *Anal. Bioanal. Chem.* **2013**, *405*, 1479–1495. [[CrossRef](#)]



© 2020 by the authors. Licensee MDPI, Basel, Switzerland. This article is an open access article distributed under the terms and conditions of the Creative Commons Attribution (CC BY) license (<http://creativecommons.org/licenses/by/4.0/>).